Measurement 236 (2024) 115111

Contents lists available at ScienceDirect

Measurement

journal homepage: www.elsevier.com/locate/measurement

Experimental research and optimization based on response surface methodology on machining characteristics of cast Al-7Si-0.6 Mg alloy: Effects of cutting parameters and heat treatment

Cem Alparslan, Şenol Bayraktar *

Recep Tayyip Erdoğan University, Faculty of Engineering and Architecture, Mechanical Engineering, Türkiye

ARTICLE INFO

Keywords:
Al-Si-Mg alloy
Microstructure
Mechanical features
Milling
BUE
BUL

ABSTRACT

In this study, structural, mechanical and machining features of Al-7Si-0.6 Mg alloy manufactured by permanent mold casting (PMC) in both as-cast (AC) and T6 heat-treated (HT) conditions were investigated. Structural and mechanical properties were determined using conventional methods. Milling experiments were conducted with titanium aluminum nitride (TiAlN) coated carbide end mills in CNC milling machine under conditions of three different cutting speeds (*V*: 50, 80 and 110 m/min), feed rate (*f*: 0.08; 0.16 and 0.24 mm/rev) and constant depth of cut (DoC) (1.5 mm). It was seen that structure of AC Al-7Si-0.6 Mg comprised of aluminum-rich α-Al, coral-like eutectic Al-Si, primary Si, Mg_2Si, Fe-rich plate, acicular β-Fe (β-Al_5FeSi) and script-like π-Fe (π-AlSiMgFe) intermetallic phases. Eutectic Al-Si, primary Si, β-Fe and π-Fe phases in the structure of the alloy in the HT condition were partially dissolved and turned into an agglomerated and spherical state. While the hardness (HB), yield (YS) and tensile strength (TS) of the alloy raised with HT, the elongation to fracture (EF) reduced. While cutting force (CF), surface roughness (SR), built-up layer (BUL) and built-up edge (BUE) decreased with increasing *V*, they increased with increasing *f* in the milling of both cast and HT alloys. Adhered layers and feed marks were consisted of the cutted surfaces of the alloys. While the most adhered layer was observed in AC alloys at a low *V* (50 m/min) and high *f* (0.24 mm/rev) combination, the least adhered layer formation was observed at the highest *V* and the lowest *f* value in HT alloys. Optimum parameters with Response Surface Methodology (RSM) were determined as *V*: 125 m/min and *f*: 0.04 mm/rev in AC and HT cases. The statistical significance of *V* and *f* on CF and SR was revealed by analysis of variance (ANOVA), while mathematical models were improved to predict CF and SR.

1. Introduction

The increase in important problems such as the energy crisis and environmental pollution around the world necessitates the automotive industry to adopt an ecofriendly orientation. The data reveals that every 10 % reduction in automobile weight reduces fuel consumption by 8 % and environmentally harmful exhaust emissions by 4 % [1]. This situation reveals the necessity of reducing the weight of automobiles to reduce environmental damage and energy consumption [2–5].

Today, Al-Si-based alloys are among the materials used for lightness in manufacturing of engine blocks, cylinder heads [6] and pistons in automotive sector [7]. These alloys are also generally preferred in the aerospace sector due to their low cost, high specific strength, wear and corrosion resistance, recyclability, castability and weldability [8,9]. They have a low coefficient of thermal expansion, good heat resistance and relatively high tensile strength (TS) [10,11]. Magnesium (Mg) is added to provide age hardening due to Mg-Si precipitation in Al-Si-Mg materials [12]. Conversely, the ductility and fracture toughness of the materials decrease depending on the increase in the Mg ratio [13,14]. This reveals that Mg has a substantial impact on both the age-hardenable property of the Al matrix and the structure, type and morphology of the brittle phases [14]. In general, higher Mg content reduces the ductility and toughness of the materials and increases the yield stress (YS). It causes the eutectic silicon (Si) to be more heterogeneous [15] by lowering the eutectic temperature. At the same time, the Mg content has an impact on the total volume fraction and the types of iron (Fe)-bearing phases [16] recognized as have a damaging impact on the tensile features [13,17]. The mechanical behaviour (Tensile and fracture) of Al-Si-

* Corresponding author.
E-mail addresses: cem.alparslan@erdogan.edu.tr (C. Alparslan), senol.bayraktar@erdogan.edu.tr (Ş. Bayraktar).

https://doi.org/10.1016/j.measurement.2024.115111
Received 1 April 2024; Received in revised form 28 May 2024; Accepted 10 June 2024
Available online 13 June 2024

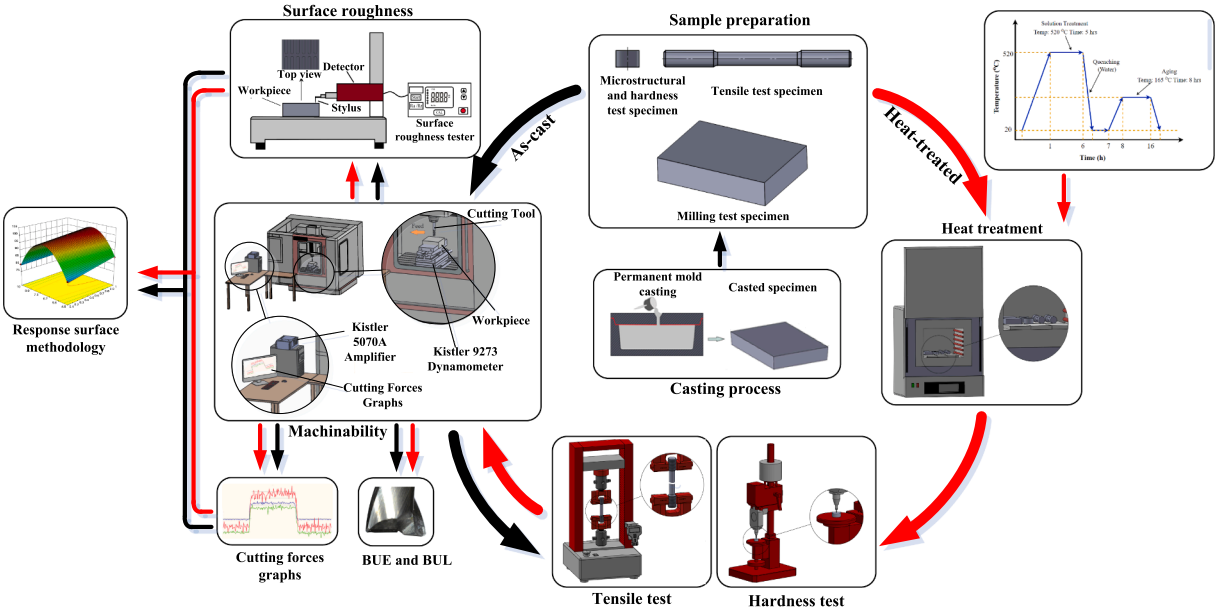

Fig. 1. Workflow diagram for experimental studies.

Mg alloys varies depending on the microstructure consisting of α-Al dendritic matrix, Fe-rich particles and eutectic Si reinforced by dispersion of Mg/Si precipitates [18]. Deteriorations in microstructure are usually caused by cracks due to Si particles. For this reason, it is important to obtain a fine and homogeneous microstructure by heat-treated (HT) to prevent these deteriorations that will adversely affect the mechanical features [19]. At the same time, depending on the raise in the Mg ratio in Al-Si-Mg alloys, precipitation hardening can be achieved by HT and their wear resistance can be improved. In other words, as a consequence of the impact of HT, the eutectic Si phases break and become globular and contribute to the increase of the bond between the hard second phase Si particles and α-Al [20]. Thus, components used in mechanical systems can have longer service lives as a result of enhanced mechanical features [21].

In industrial applications, Al-Si-Mg materials, which are generally manufactured by casting methods, must be machined to be used directly in mechanical systems. Thus, dimensional stability and desired surface quality for mechanical components can be obtained. In machinability applications, variables like cutting speed (*V*), feed rate (*f*) and depth of cut (DoC), as well as cutting tool material, coolant, and cutting tool coating material have a significant effect on outputs such as cutting force (CF), surface roughness (SR) and tool wear. These factors are controlled and optimum cutting conditions are revealed. In some of the machinability studies; Barakat et al researched drilling and tapping properties of Al-Cu (Al-6 %Cu-0.7 %Si-HT200) alloy compared to B319.1 and A356.1 alloys. It was determined that 2700 holes could be drilled without any signs of tool wear due to its high copper (Cu) content and self-lubricating feature, and built-up edge (BUE) was formed in the Al-Cu-based alloy, which would affect the hole size accuracy due to the low Si ratio. It was observed that HT200-based alloys exhibited excellent machinability properties without any signs of tool wear after 2500 holes, while wear occurred after 1600 holes in A356.1 alloy and 2160 holes in B319.1 alloy [22]. Bayraktar and Afyon investigated the effects of zinc (Zn) (4 %) and Cu (3 %) additives to Al-7Si material on torque, feed force and tool wear in drilling. Al-7Si-4Zn-3Cu alloy was seen to lowest feed force, SR, BUE and built-up layer (BUL) while this alloy had the highest machined subsurface hardness [23]. Bayraktar and Demir determined the impacts of T6 HT and cutting variables on the CF in the turning process of Al-12Si-0.6 Mg material with uncoated, physical vapour deposition-PVD-TiAlN + TiN and chemical vapour deposition-CVD-TiCN + TiN coated inserts. Their findings revealed that as the *V* increased, there was a decrease in CF, BUE, and BUL. Furthermore, HT was observed to enhance the machinability features of the alloys. In addition, uncoated inserts exhibited better machinability properties, PVD-TiAlN + TiN coated inserts performed lower, and brittle chip structure was formed by HT [21]. Bayraktar and Hekimoğlu investigated the machining properties of Al-12Si-0.1Sr material produced by PMC in turning with PVD-TiAlN coated and uncoated carbide inserts. They revealed that while the CF, SR, BUE and BUL reduced with the elevate in *V*, they raised with the elevate in *f*. Uncoated carbide inserts were found to exhibit better machinability properties [24]. Kishway et al observed that BUE and abrasive wear formed in cutting tools when machining A356 Al-Si material [25]. Gomez-Parra et al determined that two different types of wear occurred on the cutting edge of the cutting tool as BUE and BUL during the turning of Al-Cu and Al-Zn based alloys. They found that these wear mechanisms are induced by reduced cutting temperatures, chemical interaction between the cutting tool and the workpiece, and the material's ductile characteristics [26].

Maximum product quality in the manufacturing sector can be realized by controlling the outputs such as CF, SR and tool wear during machining along with optimum material selection. Today, efficient use of time and limited energy resources is an inevitable reality. It has been determined that while there have been studies regarding the machinability of Al-Si-Mg-based materials with varying element ratios but the structural, mechanical and machining properties of the Al-7Si-0.6 Mg alloy have not been investigated elaborately. Therefore, in this study, was purposed to research the structural and mechanical features of permanent mold casted (PMCed) Al-7Si-0.6 Mg material, along with machinability properties in the as-cast (AC) and T6-HT condition regarding CF, SR and tool wear in the milling process. CS and FR were optimized for minimum CF and SR using the Response Surface Methodology (RSM) technique, and mathematical models were developed for predicting experimental outcomes. The statistical significance of the independent *V* and *f* input variables on the dependent CF and SR output variables was revealed by Analysis of Variance (ANOVA) according to the $P < 0.05$ criterion in 95 % confidence level.

2. Material and method

A workflow diagram of the activities applied within the scope of the study is given in Fig. 1. It is seen that this flow diagram work consists of the processes of casting alloys, forming samples for microstructural,

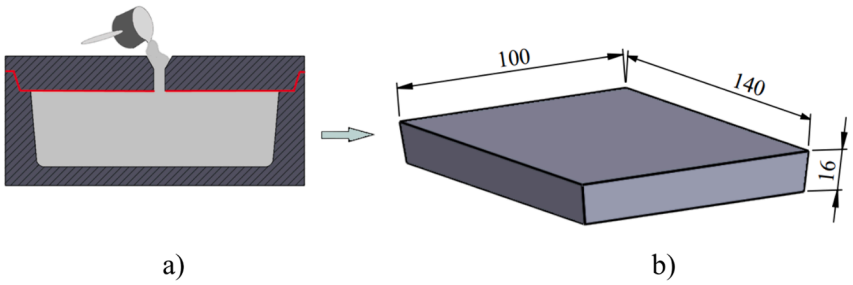

Fig. 2. Casting process, a) Permanent mold and b) Casted part (Dimensions in mm).

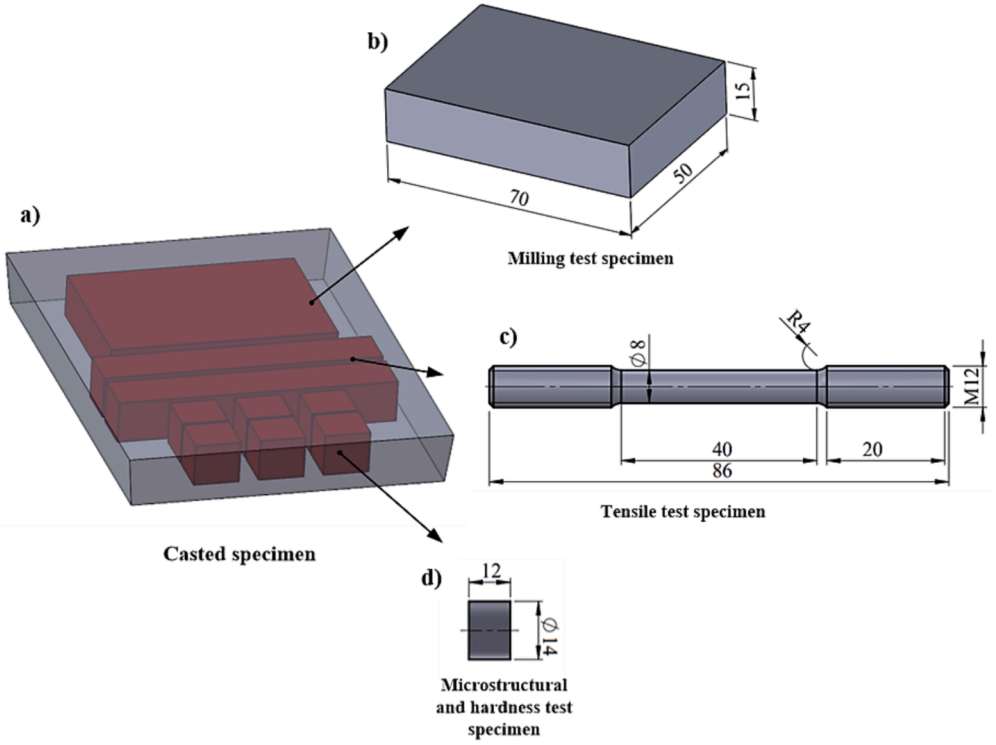

Fig. 3. Production of samples for structural, mechanical and machinability studies, a) Casted, b) Milling, c) Tensile and d) Microstructural and hardness test specimens (Dimensions in mm).

mechanical and machinability tests, HT, machinability tests, CF, SR and determination of tool wear.

In this research, Al-7Si-0.6 Mg alloy was melted in an induction melting furnace (IMF) and solidified at room temperature by pouring into a PM (Fig. 2a) at approximately 780 ± 5 °C (Fig. 2b). Al, Si, Mg, Al15Sr and AlTiB master alloys with 99.8 % purity were used in the production of the alloys. The composition of the material was analyzed in terms of weight percent with the inductively coupled plasma-optical emission spectrometry (ICP-OES) methodology.

Microstructure samples (Fig. 3d) taken from the cast workpiece were prepared for microstructural examination by being subjected to sanding, polishing and etching processes after being taken into bakelite. Microstructural studies were conducted utilizing both an optical microscope (OM-Nikon) and a scanning electron microscope (SEM-Jeol JSM 6610). Phase analyzes of the microstructure of the material were obtained using energy dispersive spectroscopy (EDS) and X-ray diffraction (XRD) techniques. XRD analyzes (Philips PW-3710) were performed on alloy samples with flat geometry utilizing a Cu-Kα radiation source (Range of scan: 20–90°, rate of scan: 3° min^{-1} and wavelength: 1.54059 Å). Hardness of Brinell (HB) values were measured in a Qness Q250CS device with a load of 62.5 kgxf and a diameter of 2.5 mm tip on the specimens whose technical drawings are given in Fig. 3d (EN ISO 6506–1:2014). Measurements were repeated ten times from different regions for each of the AC and HT samples, and final HB values were stated by calculating the arithmetic mean of these measurements. Tensile experiments were performed on alloy specimens whose technical drawings are given in Fig. 3c, using a rate of deformation $5.9x10^{-3}$ s^{-1} and 0.25 mm s^{-1} of fixed jaw (EN ISO 6892–1:2019). Three samples were produced for tensile tests from each of the AC and HT samples. The final values were obtained with an arithmetic average of the elongation to fracture (EF), YS and TS values obtained from these samples.

Milling tests for machinability properties of AC and HT alloys were performed on a 7.5 kW computer numerical control (CNC) vertical machining center (Johnford VMC 850) using the test specimens provided in Fig. 3b. *V* of 50, 80 and 110 m/min, *f* of 0.08; 0.16 and 0.24 mm/rev and constant DoC of 1.5 mm were utilized as cutting variables. These variables were stated in line with the recommendations of the cutting tool manufacturer (Sandvik coromant) as well as researches in the literature [27,28]. Additionally, the determined parameters were verified by performing preliminary cutting experiments. Milling tests carried out with TiAlN (Coefficient of friction: 0.3–0.5; coating method: PVD-900 °C; coating hardness of vickers: 3300 HV and coating thick: 3

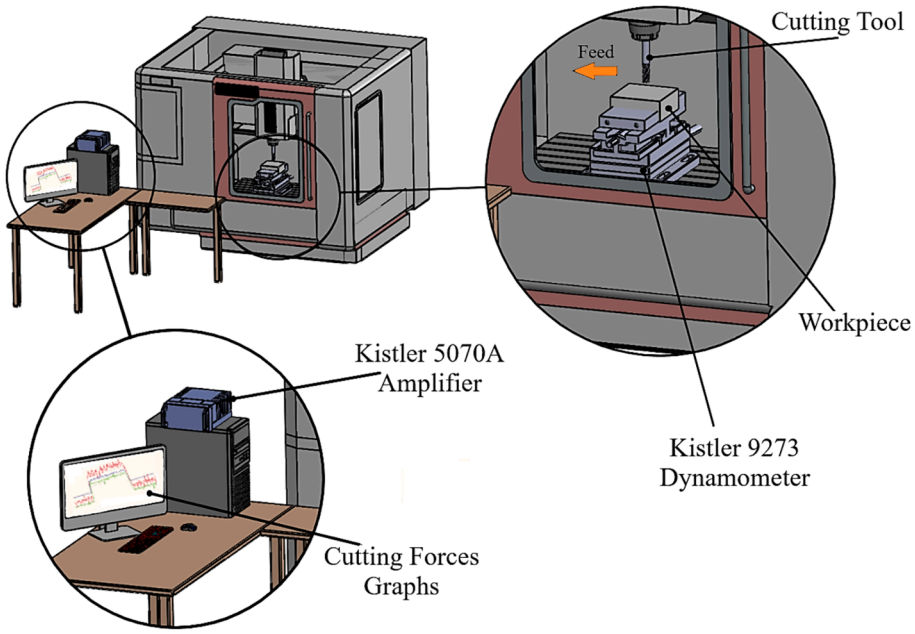

Fig. 4. Experimental test setup for milling applications.

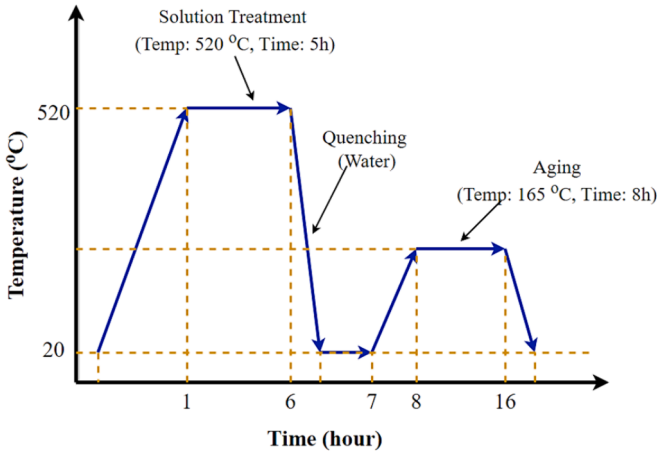

Fig. 5. T6 HT graph.

μm) coated tungsten carbide end mill (Helix angle of 30°, cutting length of 19 mm, diameter of 6 mm and number of two flutes). Kistler 9273 dynamometer, amplifier and Kistler-Dynoware software system were used to determine the CF. Forces along the different axis (X, Y and Z) were determined from the Dynoware software (Fig. 4). Final CF were calculated by resultant ($F = \sqrt{F_x^2 + F_y^2 + F_z^2}$) of these forces [29]. Machined average SR values were obtained using the Mahr Perthometer M1 tracer-tipped measuring equipment. The measurements were repeated five times and the final SR values were ascertained by calculating the arithmetic average of these measurements. International Organization for Standardization (ISO) 4287 standard, sampling length of 0.8 mm and measuring length of 4 mm were used during measurements.

T6 HT (Fig. 5) was applied on structural, mechanical and milling test specimens obtained as in Fig. 3. Protherm Mos 170/8 model furnace was used for HT. First, the specimens were solution treated at 520 °C for 5 h and quenched. The artificial ageing process was applied at 165 °C for 8 h. Studies in the literature on T6 HT applied to Al-7Si-0.6 Mg alloys were taken into account for the selection of HT parameters [30–34]. The final parameters were determined within the scope of T6 HT by creating a common combination of the parameters used in these studies [30,31].

2.1. Optimization of experimental outputs

RSM is a statistical approach that reveals the relationship between input and output variables in experimental designs based on mathematical models. Central composite design (CCD) in this technique was used as the experimental design approach, which allows the evaluation of linear impacts resulting from final quadratic interactions between different input variables [35–37]. A quadratic mathematical model was used to calculate the response resulting from interactions (Eq. (1).

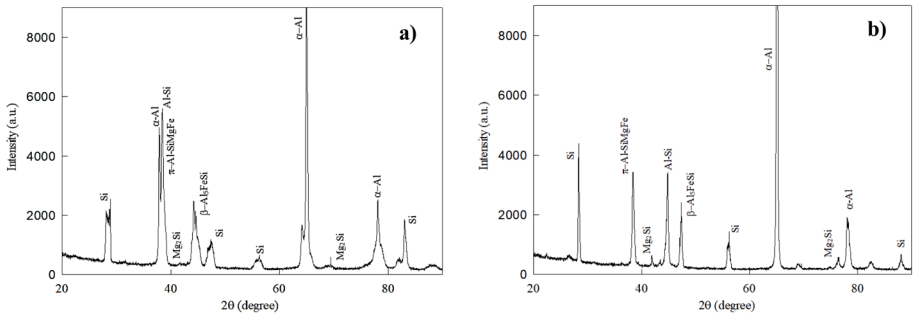

Fig. 6. XRD pattern of the alloys, a) AC and b) HT.

Table 1
Input variables and its levels.

Level	*V* (m/min)	*f* (mm/rev)
−1	50	0.08
0	80	0.16
1	110	0.24

$$Y = a_0 + \sum_{i=1}^{k} b_i X_i + \sum_{ij}^{k} b_{ij} X_{ij} + \sum_{i=1}^{k} b_{ii} X_i^2 \quad (1)$$

a_0, b_i, b_{ij}, b_{ii} ve $i, j, k = 1,2,3\ldots..n$ indicate the regression coefficients of the model, X_i and X_j are the descriptive variables, and Y is the machinability output (CF and SR) in Eq. (1). ANOVA method was used to examine the effects of input variables (V and f) on the output responses (SR and CF) [38]. The input variables and their levels used in this method are given in Table 1.

3. Results and discussion

3.1. Microstructural and mechanical properties

The chemical percent composition of Al-7Si-0.6 Mg alloy by weight was given in Table 2. The microstructure of the AC alloys was constituted of aluminum-rich α-Al, coral-like eutectic Al-Si, Mg_2Si, primary Si, and many Fe-rich plates and acicular β-Fe (β-Al_5FeSi) and script-like π-Fe (π-AlSiMgFe) intermetallic phases along the dendritic boundaries (Figs. 7 and 8). The presence of these phases was confirmed by XRD patterns (Fig. 6), OM (Fig. 7a and 8a) and SEM (Fig. 7b and 8b) images. In addition, the elemental compositions of the phases were given in Table 3 and it was determined that they were compatible with the literature [13,39,40]. The number and volume of Fe-rich phases varied depending on the Mg ratio in the alloy. While most of the Fe-rich phases were acicular β-Al_5FeSi in alloys containing approximately 0.4 % Mg by weight, π-AlSiMgFe phases with Chinese-script predominated in materials including 0.7 % Mg. In the first stage, α-Al dendrites nucleated and grew. In the second stage, the Al-Si eutectic reaction took place and depending on the decrease in temperature, a triple eutectic reaction comprising of Al, Si and β-Al_5FeSi took place. The β-Al_5FeSi was partially turned into the π-AlSiMgFe by the quasi-peritectic reaction. In the final stages, phases consisting of Al, Si, and Mg_2Si also emerged [41]. After T6 HT, it was observed that the eutectic Al-Si, primary Si, Mg_2Si, β-Fe [42] and π-Fe in the microstructure were partially dissolved and aggregated

Table 3
Chemical compositions of phases in the alloy.

Chemical composition (wt%) Phase	Al	Si	Fe	Mg
β-Al_5FeSi (Observed)	58.0—70.0	9.7—17.7	15.6—39.5	–
β-Al_5FeSi [44,45]	45.2—75.8	10.5—15.0	17.9—35.0	–
π- Al-SiMgFe (Observed)	27.4—51.1	12.8—23.3	12.2—22.0	12.3—17.5
π- Al-SiMgFe [44,45]	34.7—46.6	15.4—26.6	10—19.5	13.0—18.5
Mg_2Si (Observed)	39.3—78.2	9.7—21.2	–	1.5 – 11.6
Mg_2Si [44,45]	47.5—85.4	10.2—19.4	–	5.1—25.9

Table 2
Chemical composition of the alloy material (wt.%).

Alloy	Min/max	Si	Fe	Cu	Mn	Mg	Ni	Zn	Pb	Sn	Ti	Al
Al-7Si-0.6 Mg	Min	6.5	–	–	–	0.50	–	–	–	–	0.10	Balance
	Max	7.5	0.15	0.03	0.10	0.70	–	0.07	–	–	0.18	

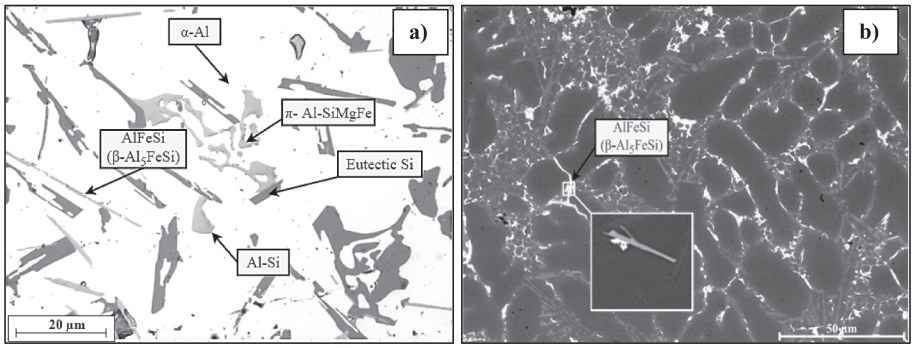

Fig. 7. Micrograph showing the structure of Al-7Si-0.6 Mg in the AC state, a) OM and b) SEM image.

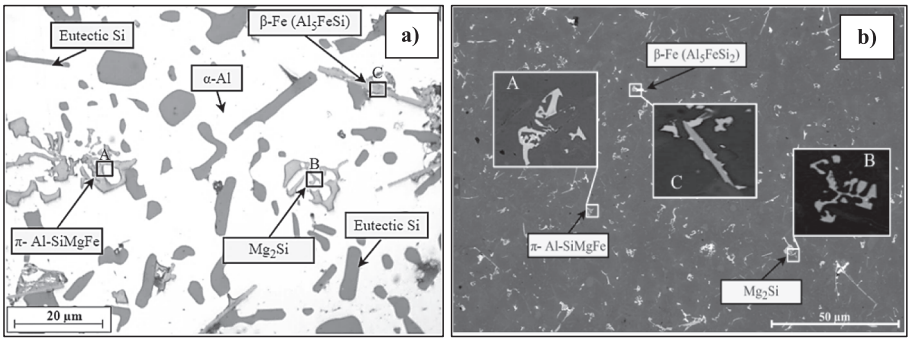

Fig. 8. Micrograph showing the structure of Al-7Si-0.6 Mg in HT state, a) OM and b) SEM image.

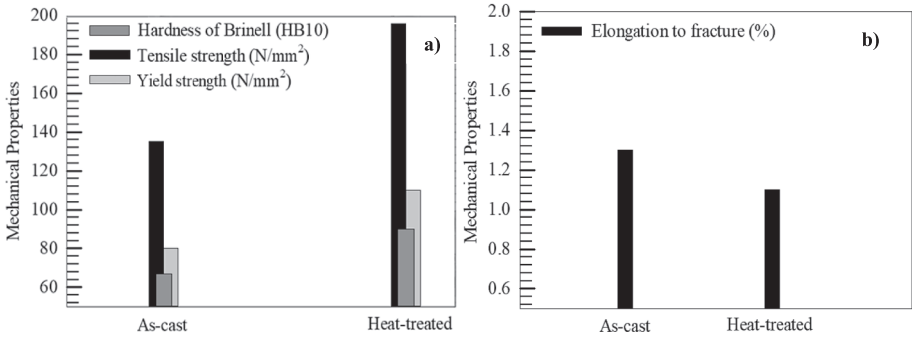

Fig. 9. Mechanical properties of Al-7Si-0.6 Mg, a) HB, TS and YS and b) EF values.

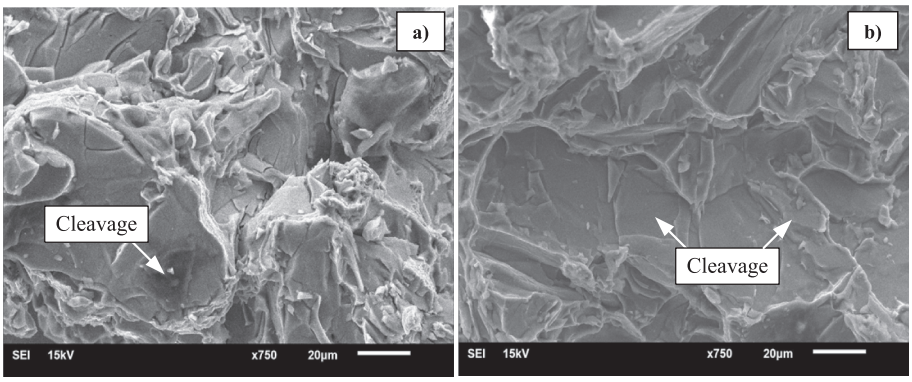

Fig. 10. SEM images of fracture surface, a) AC and b) HT.

and became spherical by coarsening (Fig. 8). The largely precipitated Mg_2Si during solidification generally reaches limit solubility within the α-Al matrix of Mg in alloys with high Mg [39]. Thus, the diffusion resistance of the alloy increases and only the Mg_2Si can be dissolved during solution HT, while the intermetallic phases remain largely unchanged [32]. However, in this study, it is thought that the partial

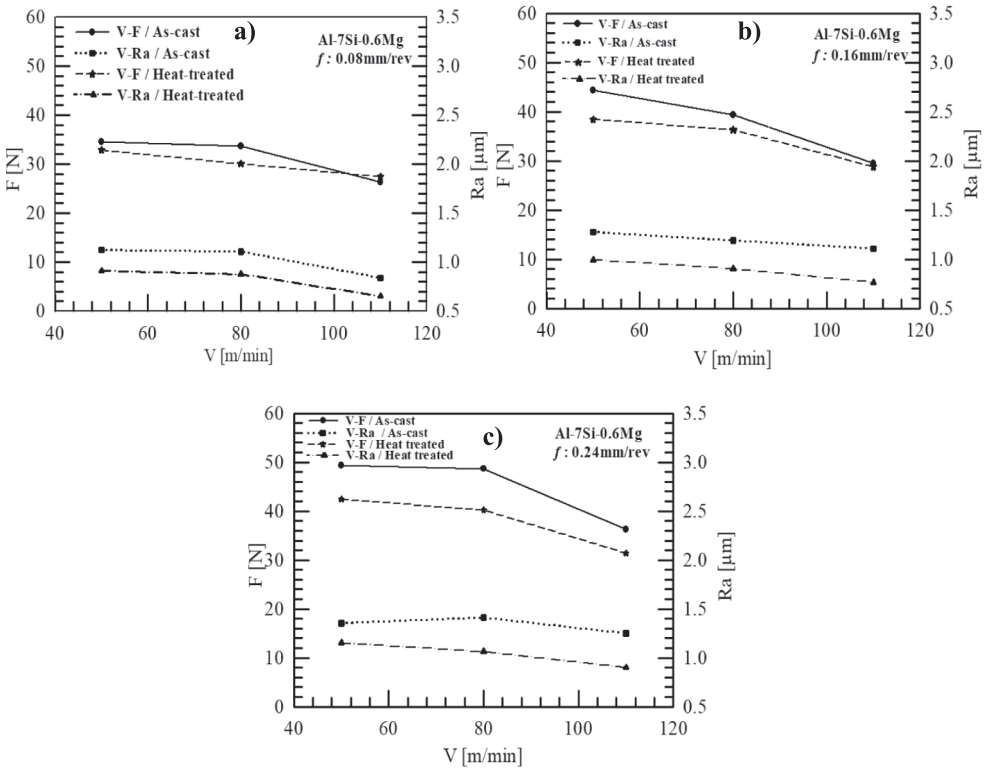

Fig. 11. V-F and V-Ra variation at constant *f* for alloy, a) 0.08; b) 0.16 and c) 0.24 mm/rev.

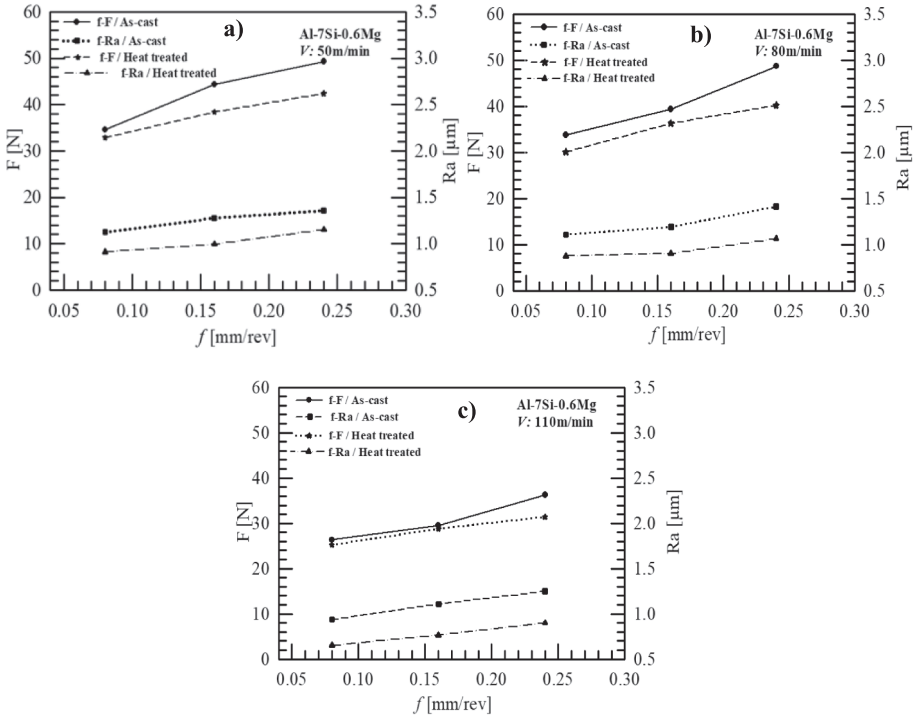

Fig. 12. V-F and V-Ra variation at constant *V* for alloy, a) 50, b) 80 and c) 110 m/min.

dissolution of the Mg_2Si after HT is due to the lower quench rate causing the loss of solute supersaturation and reducing the precipitation of Mg_2Si during artificial aging in subsequent processes [43].

Graphs showing the HB, EF, YS and TS values of AC and HT alloys were given in Fig. 9. It was seen that the HB, YS and TS (Fig. 9a) of the alloy raised with HT that the EF (Fig. 9b) reduced [46]. It was thought that solid solution hardening [20] after HT raised the HB, YS and TS values, and the increase in HB decreased the EF [21,47].

Images showing cross-sectional fracture surfaces of alloys after tensile tests were given in Fig. 10. There may be interdendritic shrinkage on the surfaces and expanding cracks in the α-Al matrix during fracture. It was thought that this crack grew up and followed over the Fe-bearing phases in the acicular structure and fracture occurred. In other words, when the material encountered an external force, it was thought that the acicular Fe-bearing phase could break readily and cause crack initiation. When the external force continued, crack growth accelerated the fracture of the alloy and the fracture surface consisting of cracks and interdendritic shrinkages appears [48]. It was seen that the fracture surfaces of the HT samples consisted of cleavage planes exhibiting brittle fracture characteristics and these planes were higher than the AC alloy. Eutectic Si particles and Fe-containing phases in the microstructure with the HT were fined according to the cast alloy, turned into spherical and homogeneously dispersed. In addition, the HB of the phases in the microstructure increased with the effect of precipitation hardening according to the HT. This increase in HB was thought to cause a decrease in EF and formed cleavage planes at the fracture surfaces [21].

T6 heat treatment involves solid solution hardening and aging processes that significantly improve the mechanical properties of the alloy. This process is accomplished by first holding the alloy at high temperatures to homogenize it and creating a supersaturated solid solution, and then rapidly cooling it with water. The cooling process ensures that the dissolved atoms are trapped in the matrix. This makes dislocation movements difficult. This process contributes to increasing mechanical properties such as Brinell hardness, yield strength and tensile strength [49–51]. Precipitates prevent dislocations, making plastic deformation more difficult. This causes the material to show more resistance under load. However, as a side effect of these hardening mechanisms, the alloy's elongation to fracture decreases. The increased brittleness of the hardened structure limits the elongation capacity of the material before it undergoes plastic deformation [52,53]. Rapid cooling after heat treatment significantly affects the grain structure of the alloy. These processes reduce the grain sizes of the alloy and increase the grain boundaries. Decreasing grain sizes and increasing number of grain boundaries make dislocation movements difficult. This helps to increase the hardness and strength of the material [54,55].

3.2. Machining features

It was revealed that CF and SR decreased with raised in *V* in the machining of AC and HT Al-7Si-0.6 Mg in constant *f* values. With the raised of *V* from 50 m/min to 110 m/min (Fig. 11) at a constant *f* of 0.08 mm/rev, the CF raised by 23.79 and 16.55 %, and the SR by 30.85 and 28.40 % (Fig. 11a), respectively, in AC and HT alloys. The CF decreased by 33.15 and 24.97 %, and the SR by 15.52 and 22.91 % (Fig. 11b), respectively, in AC and HT alloys at a constant *f* of 0.16 mm/rev. The CF reduced by 26.55 and 25.87 %, and the SR by 9.08 and 21.79 % (Fig. 11c), respectively, in cast and HT alloys at a constant *f* of 0.24 mm/rev. The temperature in the primary deformation zone increases with increasing *V*. Depending on temperature increase, the YS of alloy decreases and the creation of plastic deformation becomes easier. Therefore, it is thought that CF decreases with higher *V* [21,56,57].

It was examined that the SR decreased in general with the raised in *V*. It is thought that this is due to two different situations. The first one is the cutting edge of the cutting tool and workpiece are in contact for a shorter period of time. Secondly, the alloy with high *V* softens and the resistance to the cutting tool reduces owing to the raised temperature on the workpiece surface. Therefore, the cutting process becomes easier and a more stable and precise machined surface can be obtained [58,59]. It was examined that CF and SR rised with elevate in *f* in the machining of AC and HT material under constant *V* conditions. At a constant *V* of 50 m/min, the CF increased by 42.68 and 29.09 %, and the SR increased by 25.11 and 26.31 %, respectively, in AC and HT alloys with a raise in *f* from 0.08 mm/rev to 0.24 mm/rev (Fig. 12a). At a constant *V* of 80 m/min, the CF increased by 44.37 and 33.74, and the

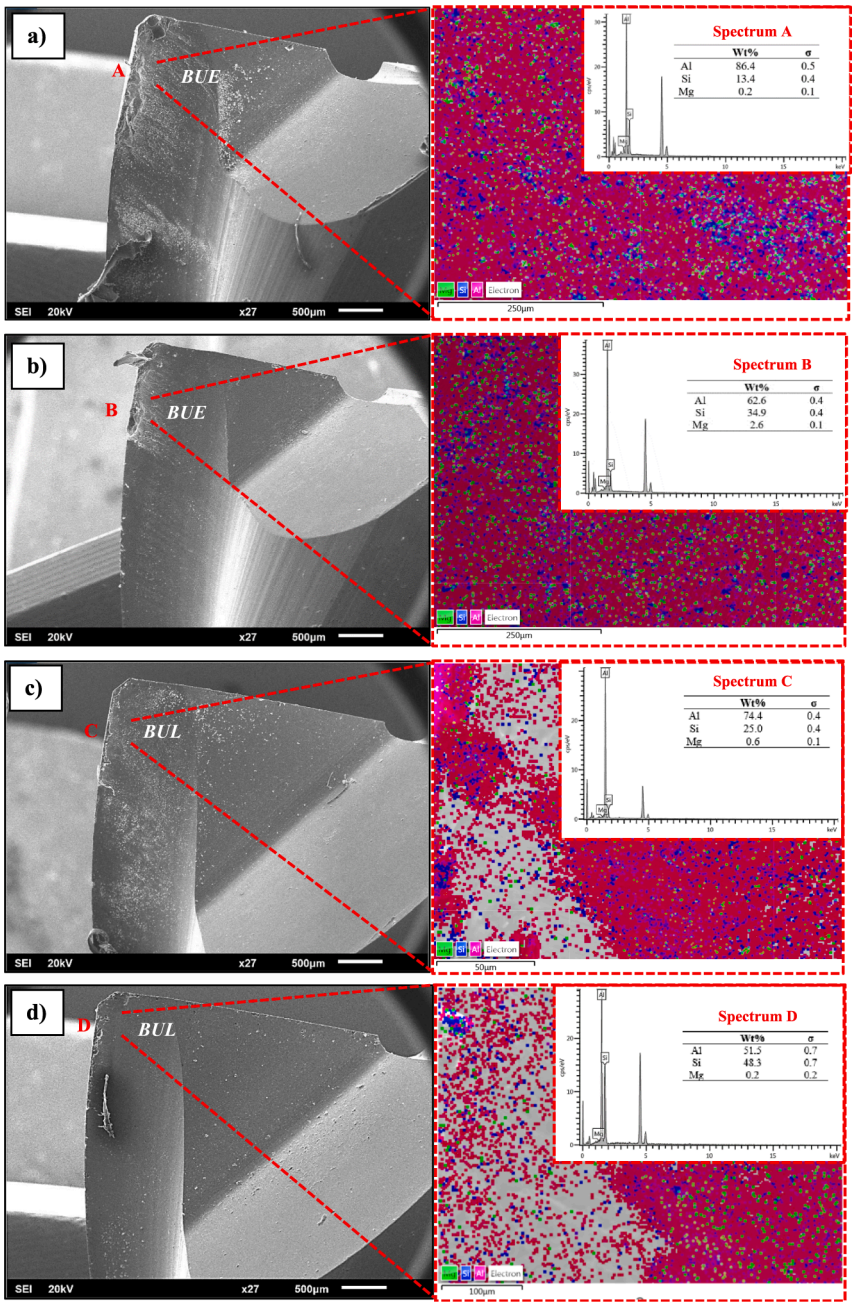

Fig. 13. EDS images of cutting tool rake face, a) AC (*V* of 50 m/min and *f* of 0.24 mm/rev), b) HT (*V* of 50 m/min and *f* of 0.24 mm/rev), c) AC (*V* of 110 m/min and *f* of 0.08 mm/rev) and d) HT (*V* of 110 m/min and *f* of 0.08 mm/rev).

SR increased by 33.48 and 21.46 % for AC and HT alloys, respectively (Fig. 12b). At a *V* of 110 m/min, CF increased 37.51 and 24.56 %, and the SR 42.22 and 37.98 %, respectively, in AC and HT alloys (Fig. 12c). As the *f* increases, the chip cross-section that needs to be cut increases and thus more power is needed. In other words, depending on the increasing chip cross-section, the tool-chip interface contact area raises and force required to overcome the shear stress increases [21,60]. The average SR increases with the increase in *f*. This situation was demonstrated in the literature with the mathematical expression $R_a = f^2/32r$. According to this expression, the terms R_a, *f* and *r* are mean surface roughness, *f* and cutting tool insert radius, respectively [61].

The primary Si, eutectic Si, Mg_2Si, π-Fe and β-Al_5FeSi in the structure of the alloy have higher hardness than the ductile α-Al phase. These hard phases significantly affect the fracture characteristics in that they facilitate crack propagation in the alloy. This situation was also revealed in the studies of Edwards et al. [18]. On the other hand, it is thought that these hard phases facilitate fracture and develop the machinability features of the material during machining. Structural damages in Al-Si-Mg materials are generally caused by microcracks due to the impact of Si particles. In this regard, the HT process is critical to obtain a fine and homogeneous microstructure in the alloy. Al-Si-Mg materials are subjected to HT to ensure precipitation hardening by adding 0.3–0.7 % Mg [19,62]. The hardness of material due to the precipitate hardening that occurs as a result of HT increases and the breakability of the chip becomes easier with the decrease in elongation to fracture during machining. This facilitates the evacuation of chip from the cutting zone and improves the machining features of the material by reducing wear on the cutting tool [21]. As seen in Figs. 11 and 12, it was stated that the HT process reduced the CF and SR in machining alloys. In other words, it improved the machinability of alloys. HT stands out as a pivotal

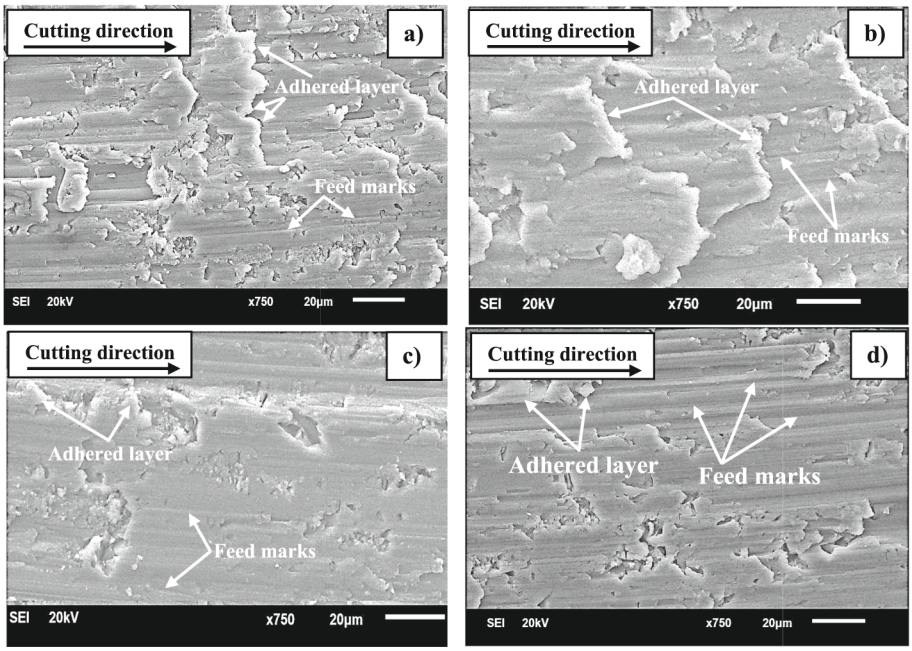

Fig. 14. SEM details of machined surfaces a) AC (*V* of 50 m/min and *f* of 0.24 mm/rev), b) HT (*V* of 50 m/min and *f* of 0.24 mm/rev), c) AC (*V* of 110 m/min and *f* of 0.08 mm/rev) and d) HT (*V* of 110 m/min and *f* of 0.08 mm/rev).

manufacturing process for enhancing the mechanical and machining features of alloys. HT develops the HB features of the alloy and reduces the formation of BUE and BUL in the cutting tool rake face, while increasing the cutted surface quality. At the same time, due to the material's high HB and low EF, it contributes to the formation of shorter and brittle chips during cutting compared to AC alloys. Short and brittle chip formation plays an active role in faster chip removal from the cutting zone by reducing the formation of BUE and BUL at the cutting edge [21]. During the machining of ductile materials, the initial stage results in the formation of BUL on the cutting tool's rake face. BUL is the smearing of ductile phases in the cutting tool rake face over a large area with the effect of mechanical and thermal stresses [63]. If this smearing continues, the chip accumulates or adheres to the rake face and turns into BUE. BUE causes distortion in the cutting tool geometry and breakage of the cutting edge. This makes the cutting process difficult and rises the CF and SR. In this study, the worst machinability conditions (*V* of 50 m/min and *f* of 0.24 mm/rev) were observed in the machining of AC alloys at the lowest *V* and highest feed parameters (Fig. 11c and Fig. 12a), while the best machinability outputs (*V* of 110 m/min and *f* of 0.08 mm/rev) were obtained under high *V*, low *f* and HT conditions (Fig. 11a and Fig. 12c).

BUE occurred in the cutting tool's rake face in the milling of the materials under the worst machining conditions, while BUL occurred during the machining under the best machining conditions. BUL formation is closely related to the initial molten metal matrix extrusion due to the impact of soft phases (α-Al) depending on compression forces between the tool and chip in the first stage during machining. This was also supported by the EDS images in Fig. 13. The chip sweeps the Al-Si-Mg remnants (Fig. 13) and induces BUL in the tool's rake face during cutting. It also causes the formation of adhered layers and feed marks on the surface of the machined (Fig. 14). Si, Mg and Fe-rich phases have higher melting points than the ductile α-Al phase. It remains solid during cutting and many of these phases are removed with the chip. The amount of these hard phases can increase in the conversion of BUL to BUE and they act as carriers in the formation of BUE. The thickness of the BUL depending on the continued cutting process increases and this layer turns into BUE (Fig. 13a and b). It is accepted that the hardness of this layer formed is lower than the cutting tool hardness. This is thought to reduce cutting temperatures and cause BUE on the cutting tool rake face and more adhered layers (Fig. 14a and b) on the machined surface. Concurrently, it is thought that the adherent BUE on the rake face causes the tool geometry to deteriorate and reduces the quality of the machined surface with the impact of the ductile α-Al phase on the machined surface [63]. It was found that these layer formations decreased compared to AC alloys (Fig. 13c and d, Fig. 14c and d) due to the increase in the HB of the alloys and the reduce in the EF with HT [21]. At the same time, it

Table 4
SR and CF results for AC and HT materials.

AC material				
	Input variables		**Output responses**	
Test No	***V* (m/min**	***f* (mm/rev)**	**SR (µm)**	**CF (N)**
1	80	0.16	0.99	39.34
2	50	0.16	1.08	44.32
3	80	0.16	1.01	39.55
4	80	0.24	1.21	48.70
5	50	0.08	0.92	34.57
6	110	0.08	0.65	27.43
7	110	0.24	1.05	36.23
8	80	0.16	1	40.17
9	110	0.16	0.91	29.54
10	80	0.16	0.98	40.01
11	80	0.16	1.03	39.81
12	50	0.24	1.16	49.33
13	80	0.08	0.908	33.73
HT material				
	Independent variables		**Output response**	
Test No	***V* (m/min**	***f* (mm/rev)**	**SR (µm)**	**CF (N)**
1	80	0.16	0.90	36.32
2	50	0.16	0.99	38.43
3	80	0.16	0.91	36.23
4	80	0.24	1.06	40.23
5	50	0.08	0.91	32.88
6	110	0.08	0.64	26.35
7	110	0.24	0.90	31.46
8	80	0.16	0.88	37.24
9	110	0.16	0.77	28.84
10	80	0.16	0.91	36.35
11	80	0.16	0.89	36.98
12	50	0.24	1.15	43.44
13	80	0.08	0.876	30.08

Table 5
ANOVA results for SR in AC material.

Source	Degree of freedom	Sum of square	Mean of square	F	P	Observation
Model	5	0.221	0.044	30.610	0.000	Significant
Lineer	2	0.203	0.101	70.220	0.000	Significant
V	1	0.052	0.052	36.100	0.001	Significant
f	1	0.151	0.151	104.34	0.000	Significant
Square	2	0.011	0.005	3.810	0.076	Not Significant
*V*V*	1	0.009	0.009	6.840	0.035	Significant
*f*f*	1	0.000	0.000	0.030	0.862	Not Significant
2-Way interaction	1	0.007	0.007	4.990	0.061	Not Significant
*V*f*	1	0.007	0.007	4.990	0.061	Not Significant
Error	7	0.010	0.001	–	–	–
Lack of fit	3	0.008	0.002	7.800	0.038	Significant
Pure error	4	0.001	0.000	–	–	–
Total	12	0.231	–	–	–	–
R^2: 95.63 %; R^2(Adj):92.50 %; R^2(Pred):73.05 %						
ANOVA results for CF in AC material						
Model	5	524.387	104.877	69.510	0.000	Significant
Lineer	2	478.694	239.347	158.640	0.000	Significant
V	1	217.202	217.202	143.970	0.000	Significant
f	1	261.492	261.492	173.320	0.000	Significant
Square	2	39.739	19.870	13.170	0.004	Significant
*V*V*	1	37.613	37.613	24.930	0.002	Significant
*f*f*	1	0.977	0.977	0.650	0.448	Not Significant
2-Way interaction	1	5.954	5.954	3.950	0.087	Not Significant
*V*f*	1	5.954	5.954	3.950	0.087	Not Significant
Error	7	10.561	1.509	–	–	–
Lack of fit	3	10.109	3.370	29.800	0.003	Significant
Pure error	4	0.452	0.113	–	–	–
Total	12	534.948	–	–	–	–
R^2: 98.03 %; R^2(Adj): 96.62 %, R^2(Pred): 81.96 %						

Table 6
ANOVA results for SR in HT material.

Source	Degree of freedom	Sum of square	Mean of square	F	P	Observation
Model	5	0.172	0.034	62.120	0.000	Significant
Lineer	2	0.164	0.082	148.240	0.000	Significant
V	1	0.088	0.088	160.040	0.000	Significant
f	1	0.075	0.075	136.430	0.000	Significant
Square	2	0.007	0.003	7.050	0.021	Significant
*V*V*	1	0.004	0.004	8.340	0.023	Significant
*f*f*	1	0.006	0.006	11.030	0.013	Significant
2-Way interaction	1	0.000	0.000	0.050	0.838	Not Significant
*V*f*	1	0.000	0.000	0.050	0.838	Not Significant
Error	7	0.003	0.000	–	–	–
Lack of fit	3	0.003	0.001	6.280	0.054	Not Significant
Pure error	4	0.000	0.000	–	–	–
Total	12	0.176	–	–	–	–
R^2: 97.80 %; R^2(Adj):96.22 %; R^2(Pred):83.90 %						
ANOVA results for CF in HT material						
Model	5	255.138	51.028	63.240	0.000	Significant
Lineer	2	223.691	111.846	138.620	0.000	Significant
V	1	121.680	121.680	150.800	0.000	Significant
f	1	102.011	102.011	126.430	0.000	Significant
Square	2	20.787	10.393	12.880	0.005	Significant
*V*V*	1	13.355	13.355	16.55	0.005	Significant
*f*f*	1	1.273	1.273	1.580	0.249	Not Significant
2-Way interaction	1	10.660	10.660	13.210	0.008	Significant
*V*f*	1	10.660	10.660	13.210	0.008	Significant
Error	7	5.648	0.807	–	–	–
Lack of fit	3	4.819	1.606	7.750	0.038	Significant
Pure error	4	0.829	0.207	–	–	–
Total	12	260.786	–	–	–	–
R^2: 97.83 %; R^2(Adj): 96.29 %, R^2(Pred): 83.10 %						

was determined that the HT and hard Fe-bearing phases in the microstructure contributed to the easy chip breakage during cutting and minimized the contact between the tool and the chip, reducing the formation of BUE and BUL (Fig. 13c and d).

3.3. ANOVA, mathematical modeling and prediction of experimental outputs

ANOVA and mathematical modeling studies were applied using Minitab 17.0 software. Regression equations created within the scope of mathematical models were used to state the variation between input and output variables. In addition, dependent variable outputs could be

Table 7
Goals and other variable ranges for optimization of CF and SR in AC and HT materials.

Constraints for AC material Variables	Goal	Lower limit	Upper limit	Weight	Significance
V (m/min)	Limit range	50	110	1	1
f (mm/rev)	Limit range	0.08	0.24		
SR (μm)	Minimum	0.650	1.210		
CF (*N*)	Minimum	27.43	49.33		
Constraints for HT material					
V (m/min)	Limit range	50	110	1	1
f (mm/rev)	Limit range	0.08	0.24		
SR (μm)	Maximum	0.640	1.15		
CF (*N*)	Minimum	26.35	43.44		

predicted at input variable values that were not tested with these equations [64]. ANOVA is used to state the statistical significance of input variables on output variables. Statistical importance is determined based on $P < 0.05$ and 95 % confidence level. It also contributes to the determination of mathematical equations, equation terms and lack of fit. [37,64–66]. The responses obtained using the RSM design are given in Table 4.

ANOVA results for SR and CF obtained as a result of machining of AC and HT materials were given in Tables 5 and 6, respectively. While V, f and $V \times V$ were determined to have statistical significance according to the $P < 0.05$ criterion on SR and CF in AC material, it was stated that $f \times f$ and $V \times f$ did not have statistical significance. While the correlation coefficients for SR in AC material were measured as R^2: 95.63 %; R^2(Adj):92.50 %; R^2(Pred):73.05 %, they were specified as R^2: 98.03 %; R^2(Adj): 96.62 %, R^2(Pred): 81.96 % for CF. These correlation coefficients showed that they were quite consistent in revealing the accuracy of the experimental outputs. The quadratic models used for SR and CF in AC material were given in Eq. (2) and (3).

$$SR_{AC}(\mu m) = 0.766 + 0.00470V + 0.36f - 0.000067V^2 + 0.65f^2 + 0.01771Vf \quad (2)$$

$$CF_{AC}(N) = 12.49 + 0.537V + 93.5f - 0.0041V^2 + 93f^2 - 0.508Vf \quad (3)$$

While V, f, $V \times V$ and $f \times f$ were determined to have statistical significance according to the $P < 0.05$ criterion on SR and CF in HT material, it was determined that $V \times f$ did not have statistical significance. While the correlation coefficients for SR in HT material were calculated as R^2: 97.80 %; R^2(Adj):96.22 %; R^2(Pred):83.90 %, for CF they were determined as R^2: 97.83 %; R^2(Adj): 96.29 %, R^2(Pred): 83.10 %. These correlation coefficients showed that there was good agreement between the experimental outputs and the statistical data. The quadratic models used for SR and CF in HT material were given in Eq. (4) and (5).

$$SR_{HT}(\mu m) = 0.915 + 0.00305V - 1.033f - 0.000045V^2 + 7.35f^2 + 0.00104Vf \quad (4)$$

$$CF_{HT}(N) = 13.10 + 0.350V + 139.9f - 0.00244V^2 - 106.1f^2 - 0.680Vf \quad (5)$$

3.4. Optimization

Independent input variables and desired output targets in the machining of AC and HT materials were determined according to minimum CF and SR values. Accordingly, optimization constraints depending on the desirability function were given in Table 7.

The input variables, responses and desirability values obtained for SR and CF according to the optimization process in AC and HT materials were given in Table 8. The independent variable values V and f in both materials for minimum SR and CF were determined as 110 m/min and 0.08 mm/rev, respectively.

Table 8
Optimum independent input parameters for *SR* and *CF* in AC and HT materials.

AC material Responses	*V* (m/min)	*f* (mm/rev)	Optimum response	Desirability
SR (μm)	110	0.08	0.669	0.952
CF (N)			26.746	0.994
HT material				
SR (μm)	110	0.08	0.658	0.951
CF (N)			25.523	0.998

Table 9
Evaluating of experimental and optimum values in AC and HT materials.

AC *V* (m/min)	*f* (mm/rev)	Response symbol	Experimental value	Optimum value	Error (%)
110	0.08	*CF*	27.430	26.102	−5.190
		SR	0.650	0.661	1.692
HT					
110	0.08	*CF*	26.35	27.485	4.307
		SR	0.640	0.669	4.531

Validation experiments were carried out at optimum input variable values for comparing experimental and optimum values. It was seen that the datas obtained were quite compatible with each other and the error rates varied between 1.692–5.190 % in AC and HT materials (Table 9).

4. Conclusions

Al-Si-Mg casting alloys are generally chosen in manufacturing of engine blocks, pistons and cylinder heads in industrial applications. After casting, it is important to apply machining operations so that these materials can be used within the desired geometric, dimension, surface tolerances and service life in mechanical systems. In this study, structural, mechanical and machininig features of Al-7Si-0.6 Mg alloy in AC and HT conditions were investigated comparatively. It is thought that the obtained data will contribute to both academic and industrial users and will guide future studies. Consequently, the results derived from the studies can be outlined in the following manner:

- The microstructure of AC Al-7Si-0.6 Mg occurred α-Al, coral-like eutectic Al-Si, primary Si, Mg_2Si, and Fe-rich plate and acicular β-Fe (β-Al_5FeSi) and script-like π-Fe (π-AlSiMgFe) intermetallic phases. The eutectic Al-Si, primary Si, Mg_2Si, β-Fe and π-Fe in microstructure of the HT alloy partially dissolved and aggregated and became spherical by coarsening.
- While the HB, YS and TS of the alloy raised with HT, the EF reduced.
- The CF, SR, BUL and BUE decreased with increasing V while increasing with increasing f in the milling of AC and HT alloys. Adhered layers and feed marks were occurred on the cutted surfaces of the alloys. While the most adhered layer was observed in AC alloys at the low V (50 m/min) and high f (0.24 mm/rev) combination, the least adhered layer formation was observed at the high V (110 m/min) and low f (0.08 mm/rev) in HT alloys.
- The optimum independent input variables were calculated as V of 110 m/min and f of 0.08 mm/rev according to the minimum SR and CF dependent output variables with RSM statistical analyze approach. It was revealed that the estimated error rates between the experimental and optimum values varied between 1.692–5.190 % and the results were quite compatible.

CRediT authorship contribution statement

Cem Alparslan: Data curation, Investigation, Software, Visualization, Writing – original draft. **Şenol Bayraktar:** Writing – review & editing, Writing – original draft, Validation, Supervision, Software, Methodology, Investigation, Conceptualization.

Declaration of competing interest

The authors declare that they have no known competing financial interests or personal relationships that could have appeared to influence the work reported in this paper.

Data availability

Data will be made available on request.

References

[1] H. Li, X. Li, The present situation and development trend of new materials used in automobile lightweight, App. Mech. Mater. 189 (2012) 58–62.
[2] P.S. Martins, J.R.G. Carneiro, E.C.T. Ba, V.F. Vieira, Study on roughness and form errors linked with tool wear in the drilling process of an Al-Si alloy under high cutting speed using coated diamond-like carbon high-speed steel drill bits, J. Manuf. Process. 62 (2021) 711–719.
[3] M. Schönemann, C. Schmidt, C. Herrmann, S. Thiede, Multi-level modeling and simulation of manufacturing systems for lightweight automotive components, Proc. CIRP 41 (2016) 1049–1054.
[4] R.A. Witik, J. Payet, V. Michaud, C. Ludwig, J.A.E. Månson, Assessing the life cycle costs and environmental performance of lightweight materials in automobile applications, Comp. Part a: App. Sci. Manuf. 42 (2011) 1694–1709.
[5] M. Zhang, Y. Tian, X. Zheng, Y. Zhang, L. Chen, J. Wang, Research progress on multi-component alloying and heat treatment of high strength and toughness Al–Si–Cu–Mg Cast Aluminum Alloys, Materials 16 (2023) 1065.
[6] P.R. Guru, F. Khan, S.K. Panigrahi, G.J. Ram, Enhancing strength, ductility and machinability of a Al–Si cast alloy by friction stir processing, J. Manuf. Process. 18 (2015) 67–74.
[7] V.M. Simões, M.C. Oliveira, H. Laurent, L.F. Menezes, The punch speed influence on warm forming and springback of two Al-Mg-Si alloys, J. Manuf. Process. 38 (2019) 266–278.
[8] Z. Liu, J. Lu, P. Zhu, Lightweight design of automotive composite bumper system using modified particle swarm optimizer, Comp. Struct. 140 (2016) 630–643.
[9] Z. Wang, X. Liu, C. Zhu, J. Xue, Z. Guo, Y. Zhang, X. Li, Influence of the interaction between Si and Sc on the microstructure and tensile properties of as casted Al-Si-Sc alloys, J. Alloys Comp. 932 (2023) 167650.
[10] D. Weiss, Improved high-temperature aluminum alloys containing cerium, J. Mater. Eng. Perform. 28 (2019) 1903–1908.
[11] Z.Y. Xiu, G.Q. Chen, X.F. Wang, G.H. Wu, Y.M. Liu, W.S. Yang, Microstructure and performance of Al-Si alloy with high Si content by high temperature diffusion treatment, Trans. Nonferr. Metals Soc. China 20 (2010) 2134–2138.
[12] G.A. Edwards, K. Stıller, G.L. Dunlop, M.J. Couper, The precipitation sequence in Al–Mg–Si alloys, Acta Mater. 46 (1998) 3893–3904.
[13] C.H. Caceres, C.J. Davidson, J.R. Griffiths, Q.G. Wang, The effect of Mg on the microstructure and mechanical behavior of Al-Si-Mg casting alloys, Metall. Mater. Trans. A 30 (1999) 2611–2618.
[14] Q.G. Wang, C.J. Davidson, Solidification and precipitation behaviour of Al-Si-Mg casting alloys, J. Mater. Sci. 36 (2001) 739–750.
[15] A.T. Joenoes, J.E. Gruzleski, Magnesium effects on the microstructure of unmodified and modified Al-Si alloys, Cast Metals 4 (1991) 62–71.
[16] B. Closset, J.E. Gruzleski, Structure and properties of hypoeutectic Al-Si-Mg alloys modified with pure strontium, Metall. Trans. A 13 (1982) 945–951.
[17] Y.H. Tan, S.L. Lee, Y.L. Lin, Effects of Be and Fe additions on the microstructure and mechanical properties of A357.0 alloys, Metall. Mater. Trans. A 26 (1995) 1195–1205.
[18] G.A. Edwards, K. Stiller, G. Dunlop, M.J. Couper, The composition of fine-scale precipitates in Al-Mg-Si alloys, Mater. Sci. Forum 217 (1996) 713–718.
[19] M. Hitchcock, Y. Wang, Z. Fan, Secondary solidification behaviour of the Al–Si–Mg alloy prepared by the rheo-diecasting process, Acta Mater. 55 (2007) 1589–1598.
[20] R. Sharma, D.K. Dwivedi, Influence of silicon (wt.%) and heat treatment on abrasive wear behaviour of cast Al–Si–Mg alloys, Mater. Sci. Eng. A 408 (2005) 274–280.
[21] Ş. Bayraktar, O. Demir, Processing of T6 heat-treated Al-12Si-0.6 Mg alloy, Mater. Manuf. Proc. 35 (2020) 354–362.
[22] H. Barakat, Y. Zedan, A.M. Samuel, H.W. Doty, S. Valtierra, F.H. Samuel, Effect of metallurgical parameters on the drilling and tapping characteristics of aluminum cast alloys, Int. J. Adv. Manuf. Technol. 105 (2019) 1357–1370.
[23] Ş. Bayraktar, F. Afyon, Machinability properties of Al–7Si, Al–7Si–4Zn and Al–7Si–4Zn–3Cu alloys, J. Braz. Soc. Mech. Sci. Eng. 42 (2020) 1–12.
[24] Ş. Bayraktar, A.P. Hekimoğlu, Performance evaluation of different carbide inserts in turning of newly developed Al-12Si-0.1 Sr alloy, Mater. Werkst. 54 (2023) 120–128.
[25] H.A. Kishawy, M. Dumitrescu, E.G. Ng, M.A. Elbestawi, Effect of coolant strategy on tool performance, chip morphology and surface quality during high-speed machining of A356 aluminum alloy, Int. J. Mach. Tools Manuf. 45 (2005) 219–227.
[26] A. Gómez-Parra, M. Álvarez-Alcón, J. Salguero, M. Batista, M. Marcos, Analysis of the evolution of the built-up edge and built-up layer formation mechanisms in the dry turning of aeronautical aluminium alloys, Wear 302 (2013) 1209–1218.
[27] T.O. Sadiq, B.A. Hameed, J. Idris, O. Olaoye, S. Nursyaza, Z.H. Samsudin, M. I. Hasnan, Effect of different machining parameters on surface roughness of aluminium alloys based on Si and Mg content, J. Braz. Soc. Mech. Sci. Eng. 41 (2019) 1–11.
[28] G.M. Uddin, F.M. Joyıa, M. Ghufran, S.A. Khan, M.A. Raza, M. Faısal, I. A. Chaudhry, Comparative performance analysis of cemented carbide, TiN, TiAlN, and PCD coated inserts in dry machining of Al alloy, Int. J. Adv. Manuf. Technol. 112 (2021) (2024) 1461–1481.
[29] A.P. Hekimoğlu, Ş. Bayraktar, Y. Turgut, Kesme Hızı ve İlerlemenin Al-35Zn Alaşımının işlenebilirliğine etkisinin incelenmesi, 2nd Int, Sympos. Innov. Appr. Sci. Stud. 2 (2018) 77–83.
[30] N.D. Alexopoulos, A. Stylıanos, Impact mechanical behaviour of Al–7Si–Mg (A357) cast aluminum alloy; The effect of artificial aging, Mater. Sci. Eng. A 528 (2011) 6303–6312.
[31] P.A.B. Machado, J.M. Do Vale Quaresma, A. Garcıa, C.A. Dos Santos, Investigation on machinability in turning of as-cast and T6 heat-treated Al-(3, 7, 12%) Si-0.6% Mg alloys, J. Manuf. Proc. 75 (2022) 514-526.
[32] X. Wu, H. Zhang, Z. Ma, T. Tao, J. Gu, W. Song, H. Zhang, Interactions between Fe-rich intermetallics and Mg-Si phase in Al-7Si-xMg alloys, J. Alloys Comp. 786 (2019) 205–214.
[33] O.S. Es-Said, D. Lee, W.D. Pfost, D.L. Thompson, M. Patterson, J. Foyos, R. Marloth, Alternative heat treatments for A357–T6 aluminum alloy, Eng. Fail. Analy. 9 (2002) 99–107.
[34] X. Dong, S. Ji, Si poisoning and promotion on the microstructure and mechanical properties of Al–Si–Mg cast alloys, J. Mater. Sci. 53 (2018) 7778–7792.
[35] A.A. Adam, H. Soleimani, J.O. Dennis, O. Aldaghri, R. Alhathlool, M.H. Eisa, K. H. Ibnaouf, B.A. Abdulkadir, F. Usman, Z.U. Zango, M.N. Isa, M.F.B.A. Shukur, A response surface methodology approach to crafting superior performance of potassium salt-based solid biopolymer electrolytes, Meas. 227 (2024) 114210.
[36] Ş. Bayraktar, A.P. Hekimoğlu, Optimization of thrust force and surface roughness using response surface methodology (RSM) in drilling of Al-30Zn alloy, Gümüşhane Uni, J. Sci. Technol. 10 (2020) 804–813.
[37] Ş. Bayraktar, Y. Turgut, Effects of WEDM and AWJ cutting methods on induction motor efficiency and total magnetic losses: Experimental design and response surface methodology, Meas. 221 (2023) 113548.
[38] C. Liu, Z. Huang, S. Huang, Y. He, Z. Yang, J. Tuo, Surface roughness prediction in ball screw whirlwind milling considering elastic-plastic deformation caused by cutting force: Modelling and verification, Meas. 220 (2023) 113365.
[39] E.A. Elsharkawi, E. Samuel, A.M. Samuel, Effects of Mg, Fe, Be additions and solution heat treatment on the p-AlMgFeSi iron intermetallic phase in Al-7Si-Mg alloys, J. Mater. Sci. 45 (2010) 1528–1539.
[40] M.Z. Wu, J.W. Zhang, Y.B. Zhang, H.Q. Wang, Effects of Mg content on the fatigue strength and fracture behavior of Al-Si-Mg casting alloys, J. Mater. Eng. Perform. 27 (2018) 5992–6003.
[41] Q.G. Wang, Microstructural effects on the tensile and fracture behavior of aluminum casting alloys A356/357, Metall. Mater. Trans. A 34 (2003) 2887–2899.
[42] L.A. Narayanan, F.H. Samuel, J.E. Gruzleskı, Dissolution of iron intermetallics in Al-Si alloys through nonequilibrium heat treatment, Metall. Mater. Trans. A 26 (1995) 2161–2174.
[43] Y.C. Tzeng, C.T. Wu, S.L. Lee, The effect of trace Sc on the quench sensitivity of Al–7Si–0.6 Mg alloys, Mater. Lett. 161 (2015) 340–342.
[44] S. Foss, A. Olsen, C.J. Sımensen, J. Tafto, Determination of the crystal structure of the π-AlFeMgSi phase using symmetry-and site-sensitive electron microscope techniques, Acta Crystal. Sec. B Struct. Sci. 59 (2003) 36–42.
[45] P.A. Rometsch, G.B. Schaffer, J.A. Taylor, Mass balance characterisation of Al-7Si-Mg alloy microstructures as a function of solution treatment time, Int. J. Cast Metals Res. 14 (2001) 59–69.
[46] C. Alparslan, Ş. Bayraktar, Comparison of Machinability Performances in Milling of Al-7Si-Mg and Al-7Si-0.6 Mg Alloys, In Int. Conf. App. Eng, Nat. Sci. (2023) 977–983.
[47] M. Zhu, Z. Jıan, G. Yang, Y. Zhou, Effects of T6 heat treatment on the microstructure, tensile properties, and fracture behavior of the modified A356 alloys, Mater. Des. 36 (2012) 243–249.
[48] Y.C. Tzeng, C.T. Wu, H.Y. Bor, J.L. Horng, M.L. Tsaı, S.L. Lee, Effects of scandium addition on iron-bearing phases and tensile properties of Al–7Si–0.6 Mg alloys, Mater. Sci. Eng. A 593 (2014) 103–110.
[49] M. Moradi, M. Nili-Ahmadabadi, B. Heidarian, Improvement of mechanical properties of AL (A356) cast alloy processed by ECAP with different heat treatments, Int. J. Mater. Form. 2 (2009) 85–88.
[50] A. Rawat, A. Kumar, A.P. Agrawal, Investigation of mechanical properties of heat-treated A356/SiC composite fabricated through stir casting technique, Mater. Today: Proc. 62 (2022) 203–208.
[51] D.A. Lados, D. Apelian, L. Wang, Aging effects on heat treatment response and mechanical properties of Al-(1 to 13 pct) Si-Mg cast alloys, Metal. Mater. Trans. B 42 (2011) 181–188.

[52] S.G. Shabestari, F. Shahri, Influence of modification, solidification conditions and heat treatment on the microstructure and mechanical properties of A356 aluminum alloy, J. Mater. Sci. 39 (2004) 2023–2032.
[53] N.F. Bazilah, M.R.M. Kamal, N.A. Maidin, Z. Marjom, M.A.M. Ali, U.H. Ahmad, T6 solutionizing heat treatment parameter of A356 alloy by investment casting, IOP Conf. Series: Mater. Sci. Eng. 834 (2020) 012005.
[54] J.H. Jeon, J.G. Jeon, M.R. Joo, J.W. Lee, D.H. Bae, Deformation behavior of an A356 alloy containing small sub-grains with wide low-angle boundary, J. Alloys Compound. 908 (2022) 164550.
[55] H.M. Wang, K. Li, G.R. Li, W.X. Su, S.S. Chou, T.T. Wu, X. Fan, Microstructure and properties of spinning deformed A356 alloy subject to the solution-DCT-aging multiplex heat treatment, J. Mater. Res. Technol. 23 (2023) 5520–5533.
[56] D. Priyadarshi, R.K. Sharma, Optimization for turning of Al-6061-SiC-Gr hybrid nanocomposites using response surface methodologies, Mater. Manuf. Process. 31 (2016) 1342–1350.
[57] B.N. Pathak, K.L. Sahoo, M. Mıshra, Effect of machining parameters on cutting forces and surface roughness in Al-(1–2) Fe-1V-1Si alloys, Mater. Manuf. Process. 28 (2013) 463–469.
[58] S.P. Dwivedi, S. Kumar, A. Kumar, Effect of turning parameters on surface roughness of A356/5% SiC composite produced by electromagnetic stir casting, J. Mech. Sci. Technol. 26 (2012) 3973–3979.
[59] M. Aamir, M. Tolouei-Rad, K. Giasin, A. Vafadar, Machinability of Al2024, Al6061, and Al5083 alloys using multi-hole simultaneous drilling approach, J. Mater. Res. Technol. 9 (2020) 10991–11002.
[60] M.P. Groover, Fundamentals of modern manufacturing: materials, processes, and systems, John Wiley & Sons, 2020.
[61] T. Özel, Y. Karpat, Predictive modeling of surface roughness and tool wear in hard turning using regression and neural networks, Int. J. Mach. Tools Manuf. 45 (2005) 467–479.
[62] A. Thirugnanam, K. Sukumaran, U.T.S. Pillai, K. Raghukandan, B.C. Pai, Effect of Mg on the fracture characteristics of cast Al–7Si–Mg alloys, Mater. Sci. Eng. A 445 (2007) 405–414.
[63] A. Yücel, Ç.V. Yıldırım, M. Sarıkaya, Ş. Şirin, T. Kıvak, M.K. Gupta, İ.V. Tomaz, Influence of MoS2 based nanofluid-MQL on tribological and machining characteristics in turning of AA T3 aluminum alloy, J. Mater. Res. Technol. 15 (2021) (2024) 1688–1704.
[64] S. Bayraktar, Y. Turgut, Determination of delamination in drilling of carbon fiber reinforced carbon matrix composites/Al 6013–T651 stacks, Measur. 154 (2020) 107493.
[65] Ç.V. Yıldırım, M. Sarıkaya, T. Kıvak, Ş¸Sirin, The effect of addition of hBN nanoparticles to nanofluid-MQL on tool wear patterns, tool life, roughness and temperature in turning of Ni-based Inconel 625, Trib. Int. 134 (2019) 443–456.
[66] E. Sap, Ü.A. Usca, M.K. Gupta, M. Kuntoglu, M. Sarıkaya, D.Y. Pimenov, M. Mia, Parametric optimization for improving the machining process of cu/mo-sicp composites produced by powder metallurgy, Materials 14 (2021) 1921.